

# Magnetic structure of coronal dark halos

J.D. Nölke<sup>1\*</sup>, S.K. Solanki<sup>1</sup>, J. Hirzberger<sup>1</sup>, H. Peter<sup>1,2</sup>, L.P. Chitta<sup>1</sup>, K.H. Glassmeier<sup>1,3</sup>, D. Calchetti<sup>1</sup>, and G. Valori<sup>1</sup>

<sup>1</sup> Max-Planck-Institut für Sonnensystemforschung, Justus-von-Liebig-Weg 3, 37077 Göttingen, Germany  
e-mail: solanki@mps.mpg.de

<sup>2</sup> Institut für Sonnenphysik (KIS), Georges-Köhler-Allee 401A, 79110 Freiburg, Germany

<sup>3</sup> Institut für Geophysik und extraterrestrische Physik, Technische Universität Braunschweig, Braunschweig, Germany

Submitted 27 August 2025

## ABSTRACT

**Context.** At low coronal temperatures around or below 1 MK distinct areas in the surroundings of active regions (AR) show emission at a level significantly below the emission coming from the quiet Sun (QS). These areas are referred to as dark halos, dark canopies, or dark moats.

**Aims.** To better understand the nature of dark halos we study the connection between the photospheric magnetic field and coronal emission at different temperatures.

**Methods.** Combining Solar Orbiter data from the high-resolution Polarimetric and Helioseismic Imager (SO/PHI) and Extreme Ultraviolet Imager (EUI) instruments allows us to identify these areas that are dark in the extreme ultraviolet (EUV) in the immediate vicinity of an AR. We probe both the photospheric magnetic field as well as the coronal intensities as a function of distance to the AR NOAA 12893.

**Results.** The dark halo has an unsigned magnetic flux density similar to the QS, but shows a strong radial dependence with distance from the AR centre. It drops by 38% from 6.1 G at the inner boundary to 3.8 G at the outer, shifting from above to below QS levels. Coronal emission  $\leq 1$  MK is  $\sim 40\%$  below QS and shows no dependence on distance to the AR centre. In contrast, at  $\geq 1.6$  MK, emission exceeds QS levels, but declines outward toward QS values. A few hot loops extend from the AR periphery across the halo, while at lower temperatures no such loops appear and short loops dominate the corona.

**Conclusions.** The reduced unsigned magnetic flux density in the outermost parts of the dark halo, below QS level, suggests that reduced coronal heating due to weak underlying magnetic flux heating could be partially responsible for the reduced emission around 1 MK. Closer to the AR, other mechanisms might lead to reduced heating. The different loops structures detected for hotter and cooler coronal temperatures likely play a crucial role in understanding coronal dark halos.

**Key words.** Sun: photosphere – Sun: corona – Sun: magnetic fields – Sun: atmosphere – (Sun:) sunspots

## 1. Introduction

At low coronal temperatures around or below 1 MK active regions (ARs) are often surrounded by extended areas of significantly reduced emission as compared to the emission coming from the quiet Sun (QS). This can be very prominently seen in data obtained by the Atmospheric Imaging Assembly (AIA; Lemen et al. 2012) onboard Solar Dynamics Observatory (SDO; Pesnell et al. 2012) at 171 Å or by the High Resolution Imager (HRI<sub>EUV</sub>) in the extreme-ultraviolet (EUV) of the Extreme Ultraviolet Imager (EUI; Rochus et al. 2020) onboard Solar Orbiter (Müller et al. 2020). These areas of reduced emission have been referred to by different names: dark canopies (Wang et al. 2011), emerging dimmings (Zhang et al. 2012), dark halos (Andretta & Del Zanna 2014), or dark moats (Singh et al. 2021). For our work we have adapted the term dark halos. Dark halos are visible at all transition region temperatures and at low coronal temperatures. However, unlike coronal holes (CHs) they cannot be distinguished from their surroundings at temperatures above 1 MK.

Several models have been proposed to explain the nature of the coronal dark halos. The model put forward by Wang et al. (2011) suggests that the dark halos show less emission due to the

presence of extreme-ultraviolet (EUV) absorbing material (i.e. neutral hydrogen or helium). However, as already shown by Andretta & Del Zanna (2014) and pointed out by Lezzi et al. (2023), the dark halos also appear darker at wavelengths longer than the edge of the Lyman continuum at 912 Å.

Singh et al. (2021) conclude that the formation of the coronal dark halos results from a specific configuration of the magnetic field: The strong magnetic field from the AR reaching over the area of the dark halos presses the underlying magnetic loops down and thus restricts them in height. According to Antiochos & Noci (1986) loops below 5 Mm can only reach temperatures up to  $10^5$  K and, consequently, do not emit in the EUV around 1 MK. As a result, the bulk of this EUV emission is missing inside the dark halos. At  $10^5$  K the dark halos would be expected to show strong emission in the AIA 304 Å channel. However, Singh et al. (2021) observed the opposite and state that further research is required. Furthermore, modern 3D models produce an abundance of (transient) short loops that reach temperatures well above  $10^5$  K (e.g. Chen et al. 2021, 2024) invalidating the argument about missing cool loops based on old model considerations.

In their most recent study, Lezzi et al. (2024) have reported a fine structure within the dark halos consisting of interconnected EUV-bright bundles and dark regions. They found this fine struc-

\* Corresponding author: J.D. Nölke e-mail: noelke@mps.mpg.de

ture also to be present in transition region lines and in Lyman-alpha. Further, its signature can be seen in magnetograms. From this, the authors conclude that coronal dark halos could have their origin in the lower solar atmosphere.

Zhang et al. (2012) and Payne & Sun (2021) observed emerging dimmings, a reduction in emission around ARs that is similar in appearance to dark halos. On the other hand, these emerging dimmings only last for several hours and it is thus not clear whether coronal dark halos and emerging dimmings are the same phenomenon. Zhang et al. (2012) explain the reduced emission at lower coronal temperatures as a result of reconnection of the existing flux with the emerging flux. This reconfiguration of the magnetic field in the corona causes plasma to heat up leading to an increase in emission at higher temperatures and a decrease in the plasma density at lower temperatures.

Chromospheric counterparts of coronal dark halos were first identified in the early 20th century by Hale & Ellerman (1903) and St. John (1911). Later, Bumba & Howard (1965) linked these chromospheric structures to dark H $\alpha$  fibrils. However, it remains unclear whether or how they are connected to the coronal dark halos.

Coronal dark halos are only one type of EUV-dark structures in the solar corona. Other known EUV-dark structures are CHs, AR outflows, and coronal voids. CHs (Waldmeier 1956, 1957) are structured by open magnetic fields and exhibit a significant flux imbalance, while the unsigned magnetic field is similar to the QS (Wiegmann & Solanki 2004). They appear dark in the EUV because due to the open field the coronal plasma is not within the corona and more energy is placed into acceleration than into heating the plasma, in contrast to ARs or the QS. Consequently, CHs are less hot and less dense (Munro & Withbroe 1972; Cranmer 2009). Thus they can best be seen as dark regions in EUV lines that form at hotter coronal temperatures. During solar activity minimum large persistent CHs are located at the poles. Around solar maximum CHs also show up at lower latitudes. They are referred to as low-latitude, equatorial, or on-disc CHs and often appear in the vicinity of magnetically complex ARs.

AR outflows are characterised by a strong blueshift in a Doppler velocity map mostly at the edge of an AR (Doschek et al. 2007; Doschek et al. 2008; Sakao et al. 2007; Harra et al. 2008). These AR outflows typically last at least a day, and are rooted in or close to strong unipolar magnetic flux regions, coinciding with quasi-separatrix layers where the magnetic connectivity undergoes rapid changes. Additionally, they are associated with areas of reduced coronal emission due to the reduced density. Some of these outflows follow open magnetic field lines that extend into the heliosphere, while others are at the footpoints of large-scale closed loops (see, e.g. Baker et al. 2009).

Coronal voids (Nölke et al. 2023) on the other hand are a QS phenomenon. These structures form above areas in the photosphere that are characterised by the absence of stronger magnetic elements. These reduced photospheric magnetic fields lead to a locally reduced heating of the solar corona and consequently to a reduced emission in the EUV.

Our study focuses on examining the magnetic field and coronal emission of the dark halos, specifically exploring their correlation with distance from the AR centre. We aim to understand how the magnetic field inside the dark halos is structured and how the large-scale field of the AR facilitates the formation of these dark halos. Additionally, we compare our findings on the dark halos with those of CHs and coronal voids.

## 2. Observations

A cross-calibration campaign for Solar Orbiter with observatories in Earth orbit was performed during the mission's cruise phase on 2021 November 5. At this time Solar Orbiter was almost along the Sun–Earth line, with an angle of only  $0.57^\circ$  and the distance to the Sun measured 0.86 au. Solar Orbiter was pointing at solar disc centre. The High Resolution Telescope (HRT; Gandorfer et al. 2018) of the Polarimetric and Helioseismic Imager (SO/PHI; Solanki et al. 2020) and the EUV instrument observed at several times during this day. In this study we consider the periods that contain co-temporal observations from both instruments. Because of the advantageous orbit position we complemented the Solar Orbiter data with observations from SDO/AIA.

### 2.1. Photospheric magnetic field observed with SO/PHI

The SO/PHI-HRT instrument observed between 22:46 and 23:34 (here and in the following all times are given in UTC) with a cadence of 2.5 minutes. In this study we used a single magnetogram. The SO/PHI spectral scan to obtain this magnetogram was started at 23:29:35 and its total duration was 66 seconds. At the observing distance of 0.86 au SO/PHI-HRT's plate scale of  $0.5''$  corresponds to 311 km/pixel on the solar surface. The selected line-of-sight (LOS) magnetogram is a level 2 data product (available on request: [sophi\\_support@mps.mpg.de](mailto:sophi_support@mps.mpg.de)) and shows the full field of view (FOV) of  $2048 \times 2048$  pixels.

### 2.2. Coronal observations with EUV and SDO/AIA

EUV's high-resolution telescope in the EUV (HRI<sub>EUV</sub>) observed between 22:58 and 23:59 with a cadence of 5 seconds. We chose a snapshot at 23:30:00 with an exposure time of 2.8 s that was taken around mid-observation of the SO/PHI-HRT magnetogram. Like SO/PHI-HRT the HRI<sub>EUV</sub> records  $2048 \times 2048$  pixels. With its slightly different plate scale of  $0.492''$  each pixel corresponds to 307 km/pixel on the Sun at the observing distance. HRI<sub>EUV</sub>'s FOV, therefore, covered  $629 \times 629$  Mm. We used level 2 data.<sup>1</sup>

The observation time at 23:30:00 onboard Solar Orbiter corresponds to an observation time on Earth of 23:31:07 due to the different light travel times. Hence, for our analysis we selected observations taken at this time from three different SDO/AIA passbands: 171Å, 193Å, and 211Å. For the 171Å and the 193Å channels observations at 23:31:09 and at 23:31:04, respectively, are used. To reduce the noise level in the 211Å channel we averaged five images, spanning one minute, around 23:31 (from 23:30:31 to 23:31:21). To study structural details we produced contrast enhanced images. Creating a contrast enhanced image requires an image with a very high signal-to-noise ratio (S/N). This was achieved by averaging a time series of 30 minutes (~180 images) for each of the three channels. Specifically, we averaged data around 23:31 that had been corrected for solar rotation. For all SDO/AIA observations we produced level 1.5 data and then additionally normalised the level 1.5 data to the exposure time. Therefore, intensities for each pixel are given in the same unit DN/s as the level 2 HRI<sub>EUV</sub> intensities.

<sup>1</sup> <https://doi.org/10.24414/z818-4163>

### 2.3. Spatial alignment of the different data sets

Since EUV has different telescopes for each of the two high-resolution channels in the EUV ( $\text{HRI}_{\text{EUV}}$ ) and in the Lyman-alpha line ( $\text{HRI}_{\text{Ly}\alpha}$ ) it can obtain simultaneous observations for the different channels. As described in Nölke et al. (2023) and Kahil et al. (2022) we aligned the SO/PHI-HRT LOS magnetogram to  $\text{HRI}_{\text{Ly}\alpha}$  because the magnetic or chromospheric network is visible in both, and then we aligned  $\text{HRI}_{\text{Ly}\alpha}$  with  $\text{HRI}_{\text{EUV}}$ . Unlike in Nölke et al. (2023) and Kahil et al. (2022) we did not apply a geometric distortion correction to the LOS magnetic field ( $B_{\text{LOS}}$ ) map because it did not noticeably improve the data quality. To remove dead pixels on the HRT detector a binary mask was applied to the  $B_{\text{LOS}}$  map and we additionally removed faulty pixels within two small squares at the right and left upper boundaries of the FOV. In the alignment process all data were re-scaled to the  $\text{HRI}_{\text{EUV}}$  plate scale and later cropped to the  $\text{HRI}_{\text{EUV}}$  FOV. As a result of this alignment, the  $B_{\text{LOS}}$  map needed to be shifted in the south-east direction and hence no magnetic field data is available in the upper part of the EUV FOV.

To align the SDO/AIA data with the  $\text{HRI}_{\text{EUV}}$  observation, we first re-projected the SDO/AIA observations onto the  $\text{HRI}_{\text{EUV}}$  frame using the SunPy routine (The SunPy Community et al. 2020). The rotation of the  $\text{HRI}_{\text{EUV}}$  image against the solar north and hence also between the  $\text{HRI}_{\text{EUV}}$  and SDO/AIA 171Å image is 21.5°. Next, we correlated the re-projected 171Å image with the  $\text{HRI}_{\text{EUV}}$  image and corrected all re-projected data for the small remaining shift between the re-projected 171Å and the  $\text{HRI}_{\text{EUV}}$  images.

## 3. Methods

### 3.1. Defining the dark halo boundaries

The Solar Orbiter  $\text{HRI}_{\text{EUV}}$  channel observed an area of 629 × 629 Mm at disc centre (see Fig. 1). Within this FOV the AR NOAA 12893 can be seen in the upper part, while the lower part shows a QS area. We define the area of the left bottom quarter below  $y = 157$  Mm and left of  $x = 314$  Mm as our reference QS. We chose this area because it is the largest QS area without dark halo patches within the FOV. We further sought to ensure that we did not include any non-QS structures: on the right an on-disc CH is present (see Fig. 2) and the bottom right contains a strong bipolar region which harbours a small pore.

We defined the threshold for the dark halo the same way as the threshold for coronal voids (Nölke et al. 2023): 75% of the mean QS intensity. Since we selected a QS area that exhibits a roughly symmetrical distribution of its EUV-intensities, the mean and median value do not differ greatly.

To obtain smooth iso-contours, we convolved the  $\text{HRI}_{\text{EUV}}$ -image with a Gaussian kernel with a full width at half maximum (FWHM) of 7.2 Mm (corresponding to a  $\sigma$  of 3 Mm or 10 pixels). We then applied the intensity threshold of 75% of the mean QS intensity to this convolved image. The dark halo was identified as the EUV-dark areas surrounding the AR. We varied the threshold slightly to test for its robustness and found that our results remain consistent against small changes. Fig. 1 shows the  $\text{HRI}_{\text{EUV}}$ -image and SO/PHI-HRT magnetogram. The contours of the dark halo patches have been projected onto both images.

### 3.2. Determining the AR's magnetic centre and creating ring plots

Since the dark halos form in proximity to ARs it is plausible to assume that a dark halo is not uniform throughout its entire structure. Therefore, to see how the properties of the dark halo are correlated with distance to the AR, we derived these values inside concentric rings around the AR.

First, we determined the magnetic centre of the AR which is used as the centre of the rings. Here we used the geometric centre or centroid which is calculated as the average position of the pixels, treating each pixel equally by considering only their coordinates and not the pixel values. This is achieved by calculating the geometric centre of all pixels with a field strength  $|B|$  of at least 100 G within 215 Mm (700 pixels) around the AR. We started at the clearly visible leading sunspot and iterated several times until the derived centre did not change any more. Next, concentric rings were drawn around this centre starting roughly at the inner boundaries of the dark halo at 92 Mm (300 pixels) distance to this centre. The rings have a width of 15 Mm (50 pixels) each on the  $\text{HRI}_{\text{EUV}}$ -image to which we have geometrically re-scaled all other images. An example of the EUV brightness in the set of rings can be seen in Fig. 3 for the average intensities of the  $\text{HRI}_{\text{EUV}}$ -image. Within each ring the average intensity or unsigned magnetic flux density was calculated either purely as a function of distance, not differentiating between individual dark halo patches, or for an individual dark halo patch, or for the brighter areas in-between the dark halo patches. For the dark halo the innermost and outermost rings are slightly larger to fully encompass the inner and outer edges of the dark halo.

## 4. Results

In this section we study the coronal emission and unsigned magnetic flux density of the coronal dark halo and the brighter areas in-between, as well as individual dark halo patches including a dark halo patch which overlaps with an equatorial CH. We determine how these properties behave as a function of distance to the AR centre.

### 4.1. Dark halo and CH overlap

The AR is surrounded by four dark halo patches, two larger ones and two smaller in size. We label the different dark halo patches DH1, DH2, DH3, and DH4 (see Fig. 1 for the labels). One of these larger dark halo patches, DH3, is a complex structure since it partially overlaps with a CH. The boundaries of the CH were identified via an intensity threshold of 40% of the median disc-intensity in the SDO/AIA 193Å channel. This CH is adjacent to the AR and a smaller separate part of the CH overlaps with a dark halo patch. The contours of both the CH and the dark halo are displayed in Fig. 2. Subsequently, to confirm whether the structure is indeed a CH, we checked for the presence of open magnetic fields. To achieve this, we conducted magnetic field extrapolations using pfsspy (Stansby et al. 2020; Yeates 2020) on the Daily Update Synoptic Frames map of 2021 November 6 taken with the Helioseismic and Magnetic Imager (HMI; Schou et al. 2012) onboard SDO, and placed seeds in the areas covered by the dark halo patch DH3 and the larger CH. We then traced the field lines from these seeds at a height of 2 Mm above the photosphere and set the source surface to 2.5 solar radii. This way we could determine that any open field originates from within the area of the CH and also from the dark-halo-CH com-

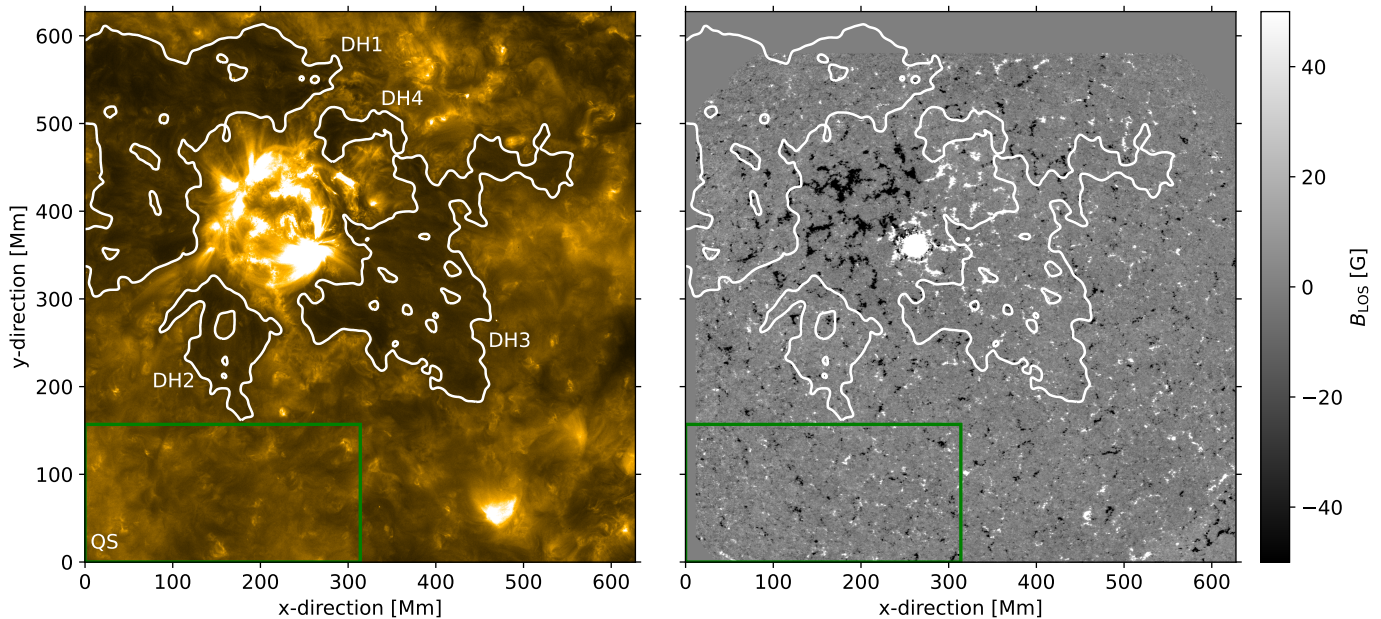


**Fig. 1.** The  $\text{HRI}_{\text{EUV}}$ -image (left) and SO/PHI-HRT-magnetogram (right). The 75% intensity contours of the dark halo are plotted in white on the  $\text{HRI}_{\text{EUV}}$ -image and are projected onto the SO/PHI-HRT-magnetogram. The individual dark halo patches are labeled in white on the  $\text{HRI}_{\text{EUV}}$  image. The green rectangle on the bottom indicates the area of the reference QS.

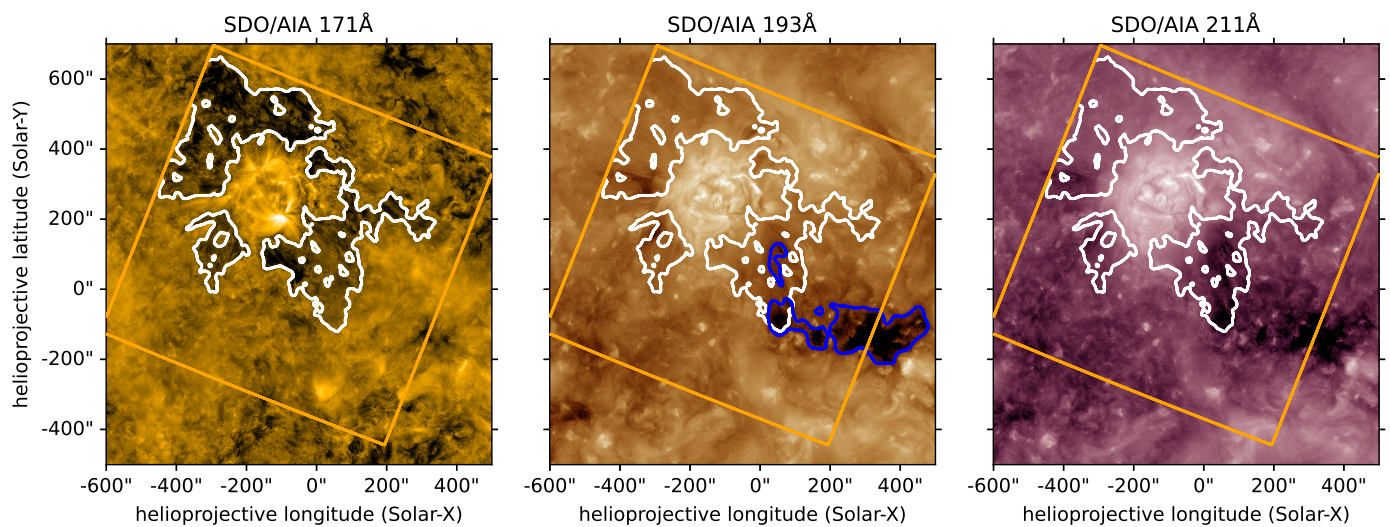


**Fig. 2.** The EUV emissions for three different SDO/AIA passbands: 171Å (left), 193Å (middle), and 211Å (right). The contours of the dark halo (white), same as in Fig. 1, have been projected onto each of the images and the orange square shows the FOV of the  $\text{HRI}_{\text{EUV}}$  observation. In the 193Å image we also show the extent of the equatorial CH (blue contour) derived by an intensity-threshold of 40% of the channels mean disc-intensity.

plex DH3. Fig. 4 displays the open field lines in green on the SDO/AIA 193Å image.

#### 4.2. Coronal emission at different temperatures

Inside the individual dark halo patches the emission in the  $\text{HRI}_{\text{EUV}}$ -channel is strongly reduced. In particular, the dark halo patches emit only between 57% and 64% of the mean emission coming from the reference QS (see Table 1 for absolute values).

##### 4.2.1. Mean-intensity's dependence on distance to AR centre

We computed the relative mean  $\text{HRI}_{\text{EUV}}$ -intensity as a function of distance to the AR centre (shown in Fig. 3), following the procedure described in Sect. 3.2. Inside each individual ring around the magnetic centre of the AR we derived the relative mean  $\text{HRI}_{\text{EUV}}$ -intensity (i.e. the mean intensity inside a ring divided by the mean intensity in the reference QS). In Fig. 3 we illustrate this for the dark halo and for the bright areas in-between. The area inside each ring is coloured according to the derived relative mean value for the area the ring covers. The dark halo and bright areas exhibit very different behaviours. On the one hand, the intensity inside the dark halo stays clearly below QS level and does not vary much. It merely increases slightly towards the

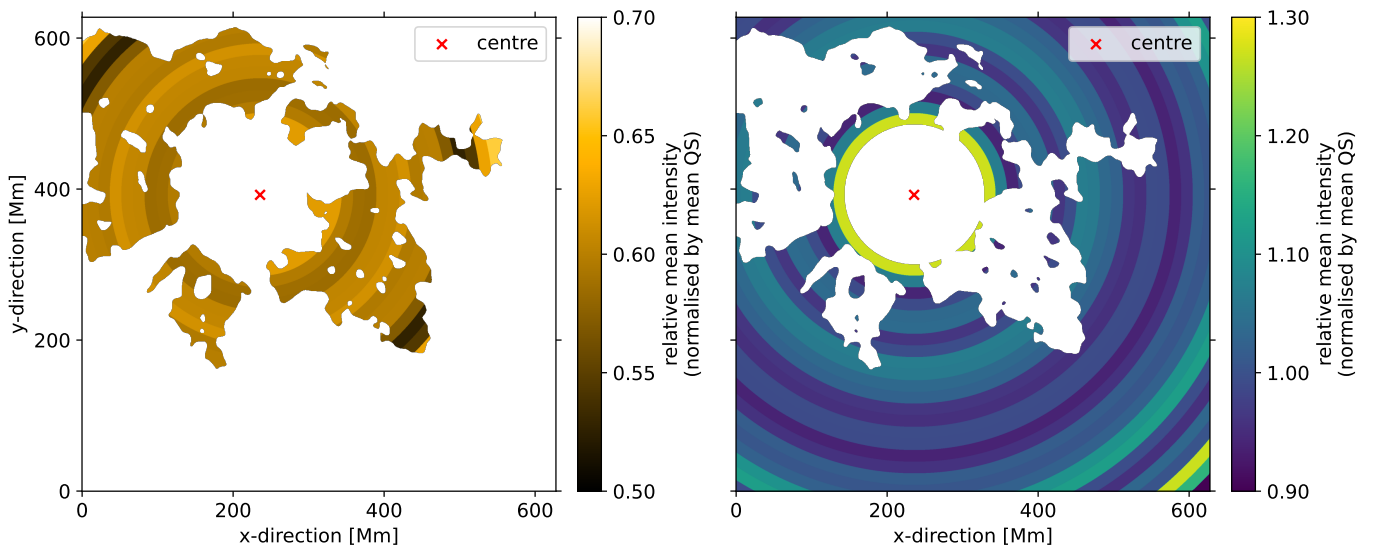


**Fig. 3.** The relative mean  $\text{HRI}_{\text{EUV}}$ -intensity inside rings around the AR obtained by dividing the mean intensity in a ring by the mean value of the reference QS. The panels on the left and on the right show the relative mean intensity inside the dark halo (i.e., we averaged over all dark halo patches at a certain distance to the AR and do not treat them separately) and for the brighter areas in-between the dark halo, respectively.

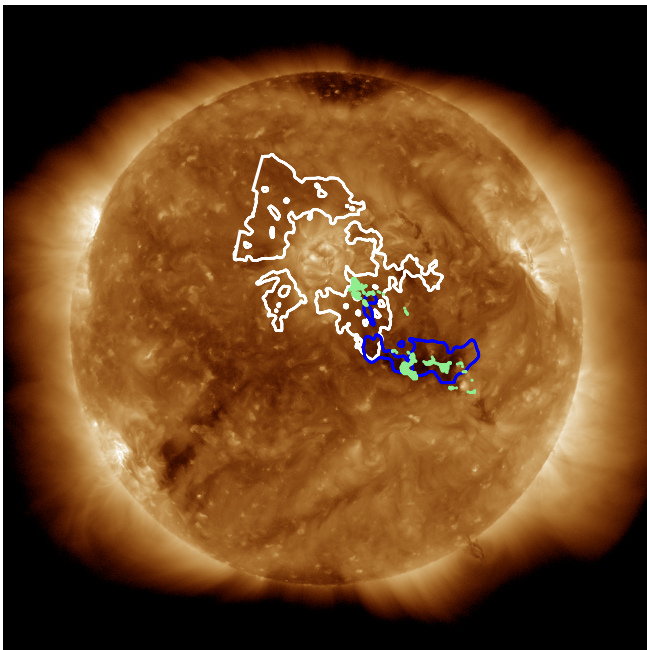


**Fig. 4.** Open magnetic field originating from the CH adjacent to the AR (blue contours), including from within the dark halo patch DH3 (white contours). The image shows the SDO/AIA 193Å channel on 2021 November 6 12:00 with the footpoints of open field lines in green.

inner and outer boundaries. The intensity in the brighter areas, on the other hand, is 1.3 times that of the QS at its inner part. With increasing distance to the AR centre the intensity then drops towards a QS-intensity level. Additionally, the rings on the bottom right, covering a bipolar region, show higher intensities again.

Radial cuts through the two areas displayed in Fig. 3 are shown in Fig. 5. The range over the dark halos is plotted from 92 – 330 Mm distance. For each value we determined the uncertainty of the mean  $\sigma_M$  as the standard deviation  $\sigma$  divided by the

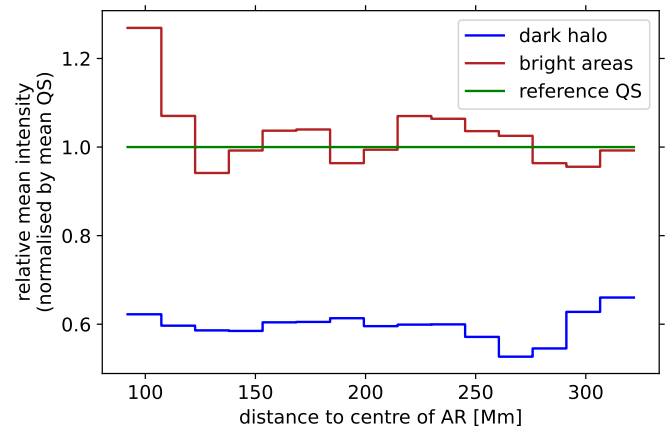


**Fig. 5.** The relative mean  $\text{HRI}_{\text{EUV}}$ -intensity as a function of distance to the AR. The mean intensity has been normalised by the mean value derived for the reference QS. The relative mean intensity inside the dark halo (blue) and for the brighter areas in-between the dark halo (dark-red) are shown. The green line denotes the value for the reference QS.

square root of the number of data points  $N$ :

$$\sigma_M = \frac{\sigma}{\sqrt{N}}, \quad (1)$$

which is small compared to the mean values measured for the intensities.

The relative mean intensities for the dark halos are clearly much lower and stay below 0.7 at all times. As described above, the relative mean intensities in the brighter region initially drop from a higher than QS values to approximately the QS value and remain relatively constant at greater distances to the AR centre. At all distances there is a difference of at least 0.3 times the QS intensity between the dark halo and the brighter areas in-between.

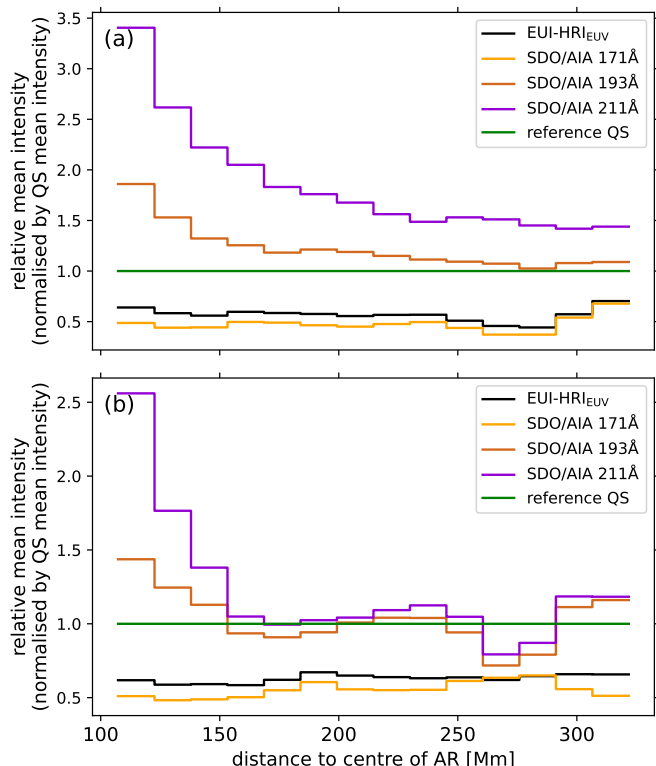


**Fig. 6.** The relative mean intensities inside individual dark halo patches as a function of distance to the AR shown for HRI<sub>EUV</sub> and the SDO/AIA 171Å, 193Å, and 211Å channels. The mean intensity has been normalised by the mean value of the reference QS of the respective channel. This mean value of the QS is indicated by the green line. Panel (a) shows the emission from DH1, and panel (b) from the dark-halo-CH complex, DH3.

#### 4.2.2. Coronal emission at different temperatures in individual dark halo patches

We further wanted to see whether individual dark halo patches behave differently, in particular if DH3, the dark-halo-CH complex, shows any significant deviation. Additionally, in order to distinguish between different dark-halo models (see Sect. 1), it is essential to understand how the relative intensity behaves at different temperatures. For this we looked at co-temporal SDO/AIA observations. We chose three different SDO/AIA-passbands: 171Å, 193Å, and 211Å. The HRI<sub>EUV</sub> and SDO/AIA 171Å channels are very similar yet not identical. While HRI<sub>EUV</sub> has a passband at 174Å and samples the solar corona at 1 MK with contributions from both the Fe IX and Fe X lines (Rochus et al. 2020), the 171Å SDO/AIA channel has most of its contributions from the Fe IX line and probes the corona just below 1 MK (Lemen et al. 2012; Peter et al. 2012). The SDO/AIA 193Å and 211Å channels see the corona at the higher temperatures of 1.6 MK, and 2.0 MK, respectively.

Iso-contours of the individual dark halo patches overlaid onto each SDO/AIA-image are shown in Fig. 2. Similarly to our approach with the HRI<sub>EUV</sub> data, we calculated the mean intensity within each ring (using the same AR centre and ring width as for the HRI<sub>EUV</sub> data). This allows us to present the relative intensity as a function of distance for the different temperature channels, as shown in Fig. 6. To have a direct comparison with the HRI<sub>EUV</sub>-channel and the reference QS, they are both included in the figure.

We conducted an analysis of the emission coming from the dark halo patch DH1 (see Fig. 6a). The 171Å SDO/AIA channel imaging cooler coronal plasma shows a rather uniformly reduced emission inside the dark halo patch, very similar to the HRI<sub>EUV</sub>-channel. At hotter temperatures the emission from the dark halo patch DH1 has a very different behaviour: For The 193Å channel the relative intensity at the inner boundary is nearly twice that of the QS in this channel. In the 211Å channel the dark halo patch is even brighter and the relative intensity is more than three times as intense as in the QS at 211Å. In both channels the relative mean intensity then decreases with increasing distance to the AR centre. Both channels exhibit emission above the QS level at all distances. At the outer boundary of the dark halo patch the relative intensities in the 193Å passband are at about the level as the QS, while the 211Å channels still shows more emission from the outer boundaries of the dark halo patch than from the mean QS.

The second dark halo patch for which we analysed the emission at different temperatures is the dark-halo-CH complex DH3 (Figure 6b). We aimed to determine whether this structure behaves differently due to its CH contribution. At coronal temperatures around 1 MK (seen by the HRI<sub>EUV</sub> and 171Å channels) DH3 shows a very similar behaviour to DH1. In the channels imaging hotter plasma (193Å and 211Å), the general trend also resembles that of DH1, showing mostly emission stronger than the QS-level and a decrease towards larger distances from the AR. However, two notable divergences are observed: at distances of 175 Mm and 280 Mm from the AR centre the intensities drop to or below the QS level before increasing again. These distances coincide with the areas where the embedded CH is located. While the CH’s presence is distinctly visible in specific locations, the overall behavior of DH3 is very similar to that of DH1.

#### 4.2.3. Bright loops over dark halos

To better highlight coronal structures in and around the dark halo patches, we applied the method described by Morgan & Druckmüller (2014) which uses a multi-scale Gaussian normalisation to enhance the image contrast. It is implemented in the python packages `sunkit_image.enhance` and we used this package to create contrast enhanced images of the three different SDO/AIA channels (visible in Fig. 7). In the enhanced image of the SDO/AIA 171Å channel bright loops originating from the periphery of the AR terminate approximately at the inner boundaries of the dark halo. There are no bright loops visible which cross over the dark halo patches or reach deep inside. At this temperature around 0.8 MK the corona is dominated by small-scale loops. Fewer of these small-scale loops appear within the dark halo than outside. The enhanced images of the passbands probing hotter plasma, on the other hand, show bright loops over the dark halo patches. Similar observations were also made by Singh et al. (2021). A discussion of their and our interpretation of this result can be found in Sect. 5.2. In detail we note that elongated brighter loops extend radially from the AR. They begin at the periphery of the AR and either cross the dark halo or terminate within it — some ending inside the halo itself or within the brighter islands it encloses. Other bright loops extend from within the dark halo, connecting either to the halo itself or to the bright islands it encloses, while some originate in these regions and stretch outward beyond the halo’s boundaries. The bright loops are rooted in strong polarity patches located inside the dark halo, the bright islands, and outside the dark halo bound-

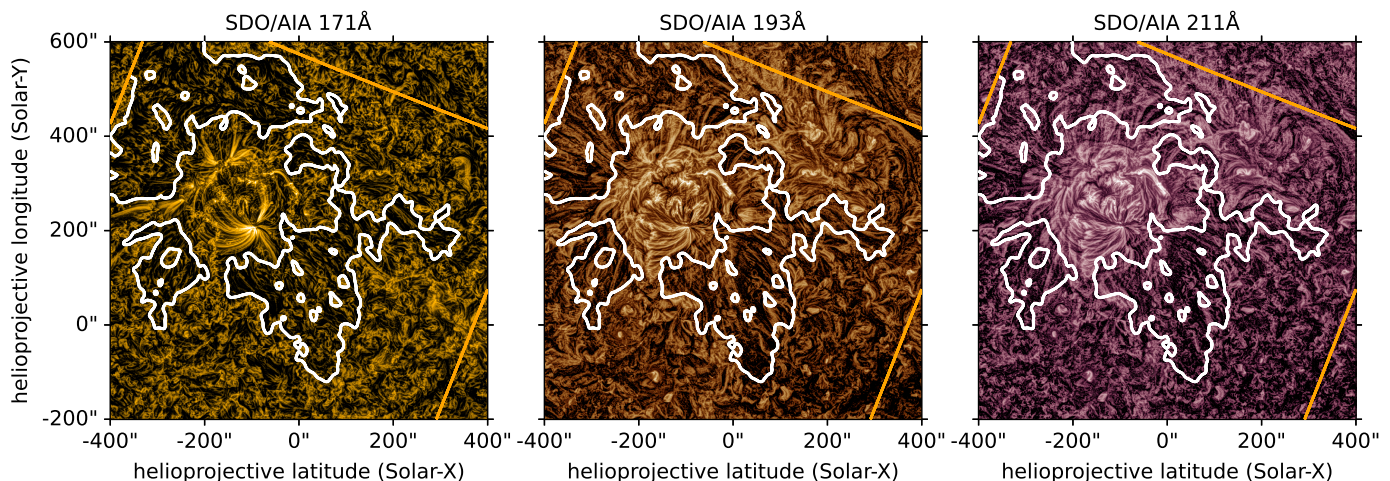


**Fig. 7.** Enhanced images of the three SDO/AIA passbands 171Å (left), 193Å (middle), and 211Å (right). The white contours outline the dark halo surrounding the AR and the orange square indicates the HRI<sub>EUV</sub>'s FOV.

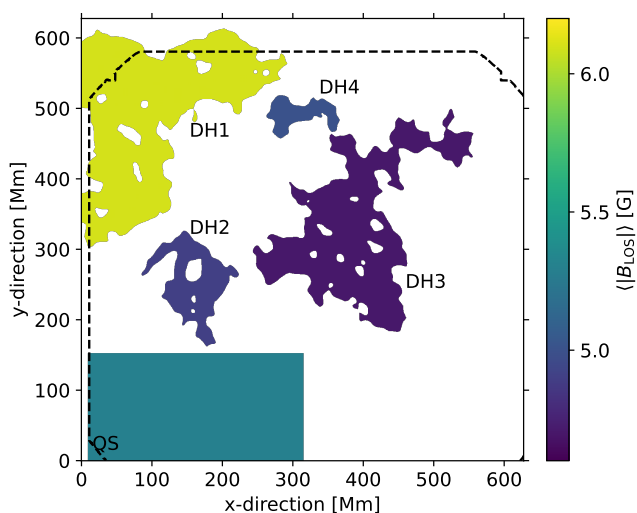


**Fig. 8.** The  $\langle |B_{\text{LOS}}| \rangle$  value above the noise level of  $1\sigma = 7.4$  G of individual dark halo patches and for the reference QS. The dashed line indicates the SO/PHI-HRT's FOV.

aries. In fact, the most of the stronger polarity patches within the dark halo and the bright islands seem to be footpoints of such bright and hot loops.

### 4.3. Photospheric magnetic field

Next, we study the photospheric magnetic field of the dark halo patches and compare it to the magnetic field of the brighter areas between them, and to the QS magnetic field.

#### 4.3.1. Average unsigned magnetic flux density

For each of the dark halo patches we derived the unsigned magnetic flux density,  $\langle |B_{\text{LOS}}| \rangle$ , individually and compared them to the reference QS. We derive the unsigned magnetic flux density as the unsigned magnetic flux  $\phi_{\text{unsigned}}$  per area  $A$ :

$$\langle |B_{\text{LOS}}| \rangle = \frac{\phi_{\text{unsigned}}}{A} = \frac{\int |B_{\text{LOS}}| dA}{\int dA} \quad (2)$$

The  $\langle |B_{\text{LOS}}| \rangle$  in each dark halo patch was obtained from the LOS magnetogram by first setting pixels below the noise level of  $1\sigma = 7.4$  G to zero (see Sinjan et al. 2022 for a sensitivity analysis of this SO/PHI-HRT data set). Next, the mean of the absolute values was calculated. This procedure yields a lower boundary estimate of the real  $\langle |B_{\text{LOS}}| \rangle$ .

The values for the individual dark halo patches are shown in Fig. 8 and listed in Table 1. The  $\langle |B_{\text{LOS}}| \rangle$  values inside dark halo patches DH2, DH3, and DH4 are slightly below the 5.3 G we derived for the reference QS. DH1 lies above this reference QS value; however, the outer parts of this particular dark halo patch are not covered by the SO/PHI-HRT magnetogram. As we will show in Sect. 4.3.2 the magnetic elements are not distributed evenly within the dark halo patch, therefore considering only a part of the dark halo could lead to a higher  $\langle |B_{\text{LOS}}| \rangle$  value. The average of all dark halo patches is 5.0 G. Therefore, the  $\langle |B_{\text{LOS}}| \rangle$  inside the dark halo patches is on average very close to that of the QS.

#### 4.3.2. Unsigned magnetic flux density's dependence on distance to AR centre

The coronal emission at higher temperatures strongly depends on the distance to the centre of the AR, see Fig. 6. Therefore, we also study the dependence of the underlying magnetic field on distance. For this, we calculated  $\langle |B_{\text{LOS}}| \rangle$  (according to Eq. 2) in rings around the AR centre in the same way as we did for the coronal intensities described in Sect. 4.2.1. Once again we determine the properties both inside the dark halo and in the brighter areas surrounding them. For both domains separately, we calculated  $\langle |B_{\text{LOS}}| \rangle$  in each ring in two different ways to obtain a lower and upper boundary for the real unsigned magnetic flux density: a) within the selected area pixels below the noise level are set to zero and then the  $\langle |B_{\text{LOS}}| \rangle$  is calculated like in Sect. 4.3.1, and b) pixels below the noise level are also included for calculating the  $\langle |B_{\text{LOS}}| \rangle$ . In the first case the real unsigned magnetic flux density is underestimated, while the latter overestimates it. Together they provide an upper and lower boundary for the real unsigned magnetic flux density.

For both the dark halo and for the brighter areas in-between we see a strong decrease away from the AR of the measured  $\langle |B_{\text{LOS}}| \rangle$ . With and without a threshold on the noise level (i.e. from both the continuous and the dashed set of lines in Fig. 9) the

**Table 1.** Unsigned magnetic flux density and coronal emission in individual dark halo patches.

Dark halo patch	$\langle  B_{\text{LOS}}  \rangle^b$ [G]	Imbalance in magnetic flux <sup>b</sup>		Emission (HRI <sub>EUUV</sub> )	
		$\Delta F$ [G]	rel. $\delta F$ [%]	abs. [DN/s]	rel. to reference QS [%]
DH1	6.1	-1.6	10	339	57
DH2	4.9	+3.0	21	381	64
DH3	4.7	+2.2	15	373	62
DH4	5.0	+5.2	37	355	59
Entire dark halo <sup>a</sup>	5.0	+0.6	4	357	60
QS	5.3	+0.8	6	599	100

**Notes.** <sup>(a)</sup> Averaged overall area covered by the dark halo patches. <sup>(b)</sup> Pixels below the 1-sigma noise level of 7.4 G are set to zero in the computation providing a lower limit for the magnetic flux density.

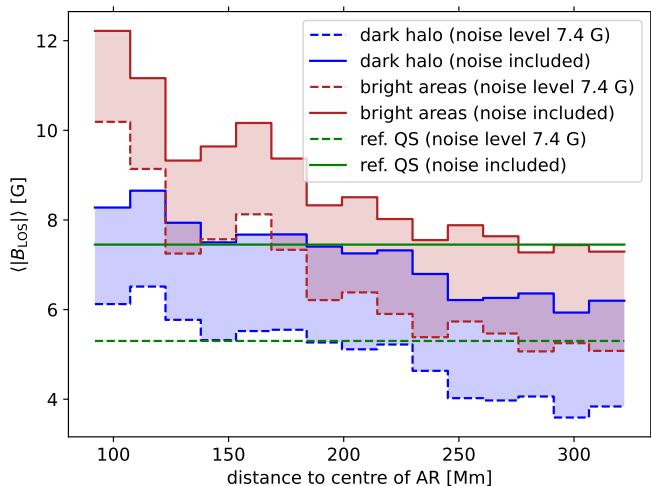


**Fig. 9.** Unsigned magnetic flux density,  $\langle |B_{\text{LOS}}| \rangle$ , in dependence of distance to the AR centre. The  $\langle |B_{\text{LOS}}| \rangle$  inside the dark halo (i.e., we averaged over all dark halo patches at a certain distance to the AR centre and do not treat them separately) is shown in blue, the red curve shows the  $\langle |B_{\text{LOS}}| \rangle$  for the bright areas in-between the dark halo patches. Dashed lines show the unsigned magnetic flux density calculated with pixels below the noise level of  $1\sigma = 7.4$  G set to zero, while the solid lines denote the unsigned flux density including pixels with values below the noise level. The real  $\langle |B_{\text{LOS}}| \rangle$  lies within the shaded areas indicated by these upper and lower boundaries. The mean value of the QS is shown in green.

relative trends, and therefore the conclusions that can be drawn, are the same. In particular, referring to the calculation with a noise level applied, Fig. 9 shows a decrease in  $\langle |B_{\text{LOS}}| \rangle$  inside the dark halo by 38% from 6.1 G to 3.8 G and inside the brighter areas by 50% from 10.2 G to 5.1 G. However,  $\langle |B_{\text{LOS}}| \rangle$  inside the dark halo is significantly lower than in the brighter in-between areas (see Fig. 9). Specifically, inside the dark halo  $\langle |B_{\text{LOS}}| \rangle$  drops below the QS level at a distance to the AR centre of 230 Mm and decreases further. In the bright in-between areas  $\langle |B_{\text{LOS}}| \rangle$  remains above the QS everywhere. The  $\langle |B_{\text{LOS}}| \rangle$  in these areas gradually trends towards the QS level with increasing distance to the AR centre. We further examined  $\langle |B_{\text{LOS}}| \rangle$  within the individual dark halo patches DH1, DH2, and DH3 (shown in Fig. 10). DH4 was excluded from the analysis due to its small size. The analysis also focused on potential differences between dark halo patches DH1 and DH2 on the one hand, and DH3 on the other, which includes the CH contribution. We can report that none were found for DH2 and DH3: both dark halo patches exhibit trends consistent with those observed for the averaged dark halo

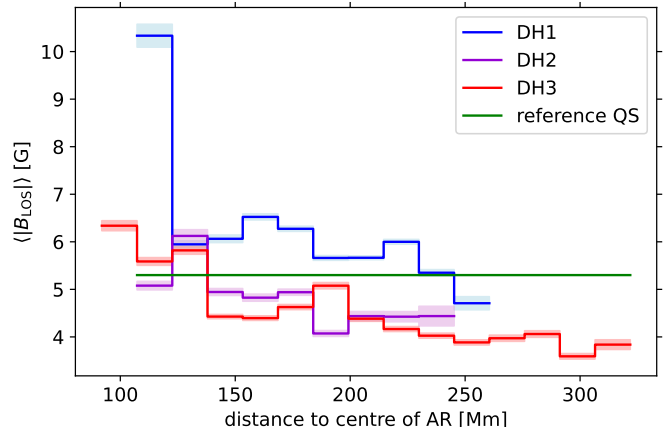


**Fig. 10.** The unsigned magnetic flux density,  $\langle |B_{\text{LOS}}| \rangle$ , as a function of distance to the AR centre for individual dark halo patches for a noise level of  $1\sigma = 7.4$  G. The values shown represent the lower limit, obtained by setting all pixels below the noise level to zero. The lighter colours denote the uncertainty of the mean  $\sigma_M$ . The mean value of the QS is shown in green.

in Fig. 9. DH1, however, deviates from this behaviour. This dark halo patch shows a very strong  $\langle |B_{\text{LOS}}| \rangle$  in the innermost ring.  $\langle |B_{\text{LOS}}| \rangle$  barely drops below the QS level, and this occurs further away from the AR centre than in the other patches. Two factors might play a role here: Firstly, the dark halo patch lies within the negative polarity region, which is much more extended than the more concentrated positive polarity. Secondly, this patch is not fully covered by the SO/PHI-HRT. It is therefore possible that, for this dark halo patch,  $\langle |B_{\text{LOS}}| \rangle$  continues to decrease with increasing distance from the AR centre. In conclusion, the common behaviour among most individual dark halo patches and the averaged dark halo is that  $\langle |B_{\text{LOS}}| \rangle$  consistently drops below the QS level.

#### 4.3.3. Flux imbalance in dark halos

To check the imbalance in the magnetic flux inside the dark halo patches, similar to Nölke et al. (2023) for coronal voids, we define the flux imbalance as the absolute value of the mean  $B_{\text{LOS}}$ :

$$\Delta F = |\langle B_{\text{LOS},i} \rangle|, \quad (3)$$

again only including pixels with field strength above the noise level  $t$ , where the spatial averages are given by  $\langle \dots \rangle$ . Similarly,

the relative imbalance in magnetic flux

$$\delta F = \frac{|\langle B_{\text{LOS},t} \rangle|}{\langle |B_{\text{LOS},t}| \rangle} \quad (4)$$

is defined as the absolute flux imbalance divided by the mean unsigned field strength. We derived the flux imbalances for the entire dark halo, but also for the large four dark halo patches separately and compared these to our reference QS area. The entire area covered by the dark halo is relatively flux balanced. The relative imbalance derived is 4% corresponding to 0.6 G. The reference QS area shows a very similar value of 6% corresponding to 0.8 G of absolute flux imbalance. The individual dark halo patches exhibit different strengths of imbalance and even different signs, which can be found in Table 1. DH1 partially overlaps with a negative polarity plage region at its innermost part, while the other dark halo patches have flux imbalances with a positive sign. The variation of these values might be due to limited statistics, as the areas covered by the individual dark halo patches are relatively small.

## 5. Discussion

### 5.1. Comparison of dark halos to CHs and coronal voids

Besides coronal dark halos, CHs and coronal voids are structures that also exhibit reduced emission in the EUV. CHs show lower emission and hence an increasing difference to their surroundings towards higher coronal temperatures. In contrast, at low coronal temperatures the dark halo studied here generally displays a uniformly reduced emission below the QS-level, while at higher temperatures its emission is significantly stronger than in the QS and decreases with distance from the centre of the AR. Thus, the emission from the dark halo patch DH1 in the 193Å and 211Å SDO/AIA channels consistently remains above or at the QS-level. At these higher temperatures an equatorial CH becomes distinctly visible in the coronal emission from the dark halo patch DH3, where two clear dips in emission correlate with the location of the CH. This creates a noticeable contrast between dark halos and CHs at higher temperatures, making higher-temperature channels useful for distinguishing between the two.

Both, the dark halo and coronal voids (Nölke et al. 2023) show a strong reduction in emission at 1 MK compared to the QS. Most of the individual dark halo patches have a  $\langle |B_{\text{LOS}}| \rangle$  that is slightly lower than that of the QS (92%–98% in DHs 2–4). The value of 120% for DH1 is because it is cut off by the SO/PHI-HRT’s FOV (see Sect. 4.3.1 and Fig. 8). In contrast, such a difference is more marked for coronal voids, where the  $\langle |B_{\text{LOS}}| \rangle$  is 76% of the value in QS (Nölke et al. 2023). However, we see a significant difference between  $\langle |B_{\text{LOS}}| \rangle$  inside the dark halo and in the bright areas surrounding the dark halo patches (see Sect. 4.3.2).

In addition to the 2021 November 5 Solar Orbiter observations, we further analysed SDO/HMI observations of 2018 April 22nd (see Appendix A) studied by Lezzi et al. (2023). The authors used a different technique to compare the magnetic field and derived the unsigned magnetic field,  $B_{\text{unsigned}}$ , which is the mean of absolute values of only those pixels above the noise level. By applying their technique and using a noise level threshold of 8 G, we derive  $B_{\text{unsigned}} = 16.1$  G for the QS and a  $B_{\text{unsigned}}$  value of 15.6 G. This value for the dark halo is slightly lower than the 17.0 G reported by Lezzi et al. (2023). The corresponding unsigned magnetic flux densities,  $\langle |B_{\text{LOS}}| \rangle$ , calculated using

Eq. 2 are 5.0 G and 6.1 G for the dark halo and QS, respectively. Qualitatively, the result is the same as for the SO/PHI-HRT data: The  $\langle |B_{\text{LOS}}| \rangle$  within the dark halo is, on average, weaker than in the QS. This difference is with 1.1 G clearly stronger in the SDO/HMI data set, while the difference in the SO/PHI-HRT data set is 0.4 G or less (excluding DH1). It is also worth noting that, in the 2018 SDO/HMI data set, the  $\langle |B_{\text{LOS}}| \rangle$  inside the dark halo remains weaker than in the QS at all distances from the AR centre, even at the inner boundary.

Dark halos typically show a systematic trend of the unsigned magnetic flux density dropping with radial distance from the AR, i.e. from their boundaries closest to the AR centre to their outer boundaries (see Sect. 4.3.2 and Appendix A). Close to the boundary to the AR the magnetic field is significantly stronger than in the QS. Then it drops to field strengths below the QS, and hence to values that compare well to coronal voids. In CHs and coronal voids the magnetic elements are more uniformly distributed than in the dark halos.

The dark halo patches show flux imbalances ranging from 10% to 37% (see Table 1 and Sect. 4.3.3). Equatorial CHs on the other hand typically show much stronger flux imbalances of at least 50% (Wiegmann & Solanki (2004) and Hofmeister et al. (2017)). DH3, which overlaps with the equatorial CH, shows no significant deviation from the other dark halo patches.

### 5.2. Nature of dark halos

We confirm the finding of Wang et al. (2011) that in the dark halos on average the  $\langle |B_{\text{LOS}}| \rangle$  is slightly weaker than in the QS. However, our detailed analysis shows a more complex picture. The  $\langle |B_{\text{LOS}}| \rangle$  drops with distance from the AR centre, and only in the outer parts of the dark halos the  $\langle |B_{\text{LOS}}| \rangle$  is weaker than the QS. Still, at the same distance from the AR centre the  $\langle |B_{\text{LOS}}| \rangle$  in the dark halo is weaker than in the bright areas between them (see Sect. 4.3.2)

The consistently lower value of  $\langle |B_{\text{LOS}}| \rangle$  in the dark halo compared to the brighter regions between them could explain why the dark halos show reduced emission by direct comparison. A weaker magnetic field is indicative of less heating of coronal plasma and hence a lower intensity from plasma around 1 MK. In the outer parts of the dark halo where the magnetic field is weaker than in the QS reduced coronal heating, similar to coronal voids in the QS (Nölke et al. 2023), could be a mechanism contributing to the reduced emission. However, while the magnetic field drops with distance from the AR centre, the emission seen in the SDO/AIA 171Å and HRI<sub>EUV</sub> channels is almost constant with distance. Moreover, because the  $\langle |B_{\text{LOS}}| \rangle$  in the inner part of the dark halo is stronger than in the QS, one would naively expect the SDO/AIA 171Å and HRI<sub>EUV</sub> emission to be stronger in the inner part of the dark halo than in the QS, in contrast to our observations. Two possible scenarios that might explain this are described below.

Firstly, the heating of the corona depends not only on the magnetic field, but also on horizontal flows, that together set the vertical Poynting flux and hence the energy flux into the corona. Smaller horizontal flows near the AR could compensate for an increasing magnetic flux and keep the heating rate stable throughout the dark halo. This would in turn lead to the uniformly reduced intensity seen in the SDO/AIA 171Å and HRI<sub>EUV</sub> channels. Future research could explore this possibility further by investigating the horizontal flows in the vicinity of ARs.

Secondly, the emission from cooler plasma ( $\leq 1$  MK), as seen in the structures in the enhanced image of the SDO/AIA 171Å channel (see Fig. 7), is organised in short loops. Within the dark halo less of these loops are visible. This is in direct contrast to plasma at higher temperatures ( $\geq 1.6$  MK) probed by the SDO/AIA 193Å and 211Å channels, where the emission is organised in longer loops that often spread radially away from the AR. Interestingly, the emission observed in these passbands probing hotter plasma exhibits a similar radial dependence to that of the magnetic field. These longer loops predominantly connect to the stronger magnetic patches within the dark halo or to the brighter islands within the dark halo structure. Hot long-ranging loops have previously also been observed by Singh et al. (2021). Their model explains the difference between the hotter and cooler plasma seen in the different passbands with strong magnetic pressure exerted onto the small-scale loops that are then confined to stable heights below 5 Mm.

## 6. Conclusions

We studied the coronal dark halo around the AR NOAA 12893. Specifically, we analysed the coronal emission at different temperatures and the photospheric magnetic field as a function of distance to the AR centre.

We report a radial profile in emission for the dark halo that varies with distance for higher coronal temperatures ( $\geq 1.6$  MK) and shows reduced emission throughout the dark halo at temperatures  $\leq 1$  MK (Sect. 4.2). Similarly, we detected variations in the unsigned magnetic flux density,  $\langle |B_{\text{LOS}}| \rangle$ , with distance (Sect. 4.3). These radial dependencies of the emission and magnetic field imply that studies should not solely rely on mean values (e.g. averages over entire dark halos), as done before.

The data set further allowed us to analyse an equatorial CH adjacent to the AR (see Sects. 4.1, 4.2.2, and 5.1). Dark halos and CHs can clearly be distinguished via their emission at different coronal temperatures because CHs show a strong contrast above 1 MK, whereas dark halos are only visible below these temperatures. This was also reported by Lezzi et al. (2023).

In Sects. 1 and 5.2 we discuss existing models explaining the dark halos and propose an additional explanation: The source regions of hotter emission ( $\geq 1.6$  MK) (Sect. 4.2.2) with visible loops over and reaching inside the dark halo (Sect. 4.2.3) are likely less dominated by the local magnetic field of the dark halo, but rather by the large-scale magnetic field of the AR. The dark halo shows a clear reduction of  $\langle |B_{\text{LOS}}| \rangle$  compared to its brighter surroundings (Sect. 4.3.2). At its outer boundaries it falls below the QS level. We suggest that reduced coronal heating due to reduced magnetic flux density might locally contribute to the dark halos dark appearance. While this could explain the reduced emission at the outer boundaries, another additional mechanism must be responsible for the reduced emission closer to the AR centre where the  $\langle |B_{\text{LOS}}| \rangle$  is stronger than in the QS.

Future work could include an analysis of horizontal flows around ARs to test whether reduced flows within a dark halo near an AR lead to a smaller Poynting flux, resulting in lower heating and thus reduced coronal emission. Obtaining new observations that include coronal spectroscopic measurements, for example from the SPICE instrument (SPICE Consortium et al. 2020), would be immensely beneficial. These data would allow us to identify potential outflows by examining Doppler shifts within a dark halo. This would help us to either identify clear boundaries of dark halos, CHs, and outflow areas or reveal where these phenomena converge, allowing for further characterisation of this

region. Studying more dark halos would also enable us to gather statistical data on the correlation between the radial distance to an AR and the  $\langle |B_{\text{LOS}}| \rangle$  or the coronal emission.

*Acknowledgements.* Solar Orbiter is a space mission of international collaboration between ESA and NASA, operated by ESA. We are grateful to the ESA SOC and MOC teams for their support. The German contribution to SO/PHI is funded by the BMWi through DLR and by MPG central funds. The Spanish contribution is funded by AEI/MCIN/10.13039/501100011033/ and European Union “NextGenerationEU”/PRTR” (RTI2018-096886-C5, PID2021-125325OB-C5, PCI2022-135009-2, PCI2022-135029-2) and ERDF “A way of making Europe”; “Center of Excellence Severo Ochoa” awards to IAA-CSIC (SEV-2017-0709, CEX2021-001131-S); and a Ramón y Cajal fellowship awarded to David Suarez-Orozco. The French contribution is funded by CNES. The EU instrument was built by CSL, IAS, MPS, MSSSL/UCL, PMOD/WRC, ROB, LCF/IO with funding from the Belgian Federal Science Policy Office (BELSPO/PRODEX PEA 4000134088, 4000112292, 4000136424, and 4000134474); the Centre National d’Etudes Spatiales (CNES); the UK Space Agency (UKSA); the Bundesministerium für Wirtschaft und Energie (BMWi) through the Deutsches Zentrum für Luft- und Raumfahrt (DLR); and the Swiss Space Office (SSO). This work was supported by the International Max Planck Research School (IMPRS) for Solar System Science at the University of Göttingen and at TU Braunschweig. This project has received funding by the European Research Council (ERC) under the European Union’s Horizon EUROPE research and innovation programme (grant agreements No. 101097844 — project WINSUN - and No. 101039844 — ORIGIN). Views and opinions expressed are however those of the author(s) only and do not necessarily reflect those of the European Union or the European Research Council. Neither the European Union nor the granting authority can be held responsible for them. This research used version 4.1.5 (10.5281/zenodo.7850372) of the SunPy open source software package (The SunPy Community et al. 2020).

## References

- Andretta, V. & Del Zanna, G. 2014, *A&A*, 563, A26  
 Antiochos, S. K. & Noci, G. 1986, *ApJ*, 301, 440  
 Baker, D., van Driel-Gesztelyi, L., Mandrini, C. H., Démoulin, P., & Murray, M. J. 2009, *The Astrophysical Journal*, 705, 926  
 Bumba, V. & Howard, R. 1965, *ApJ*, 141, 1492  
 Chen, Y., Peter, H., & Przybylski, D. 2024, arXiv e-prints, arXiv:2411.11068  
 Chen, Y., Przybylski, D., Peter, H., et al. 2021, *A&A*, 656, L7  
 Cranmer, S. R. 2009, *Living Reviews in Solar Physics*, 6, 3  
 Doschek, G. A., Mariska, J. T., Warren, H. P., et al. 2007, *The Astrophysical Journal*, 667, L109  
 Doschek, G. A., Warren, H. P., Mariska, J. T., et al. 2008, *ApJ*, 686, 1362  
 Gandorfer, A., Grauf, B., Staub, J., et al. 2018, in *Space Telescopes and Instrumentation 2018: Optical, Infrared, and Millimeter Wave*, ed. M. Lystrup, H. A. MacEwen, G. G. Fazio, N. Batalha, N. Siegler, & E. C. Tong, Vol. 10698, International Society for Optics and Photonics (SPIE), 106984N  
 Hale, G. E. & Ellerman, F. 1903, *Publications of the Yerkes Observatory*, 3, 1.1  
 Harra, L. K., Sakao, T., Mandrini, C. H., et al. 2008, *The Astrophysical Journal*, 676, L147  
 Hofmeister, S. J., Veronig, A., Reiss, M. A., et al. 2017, *The Astrophysical Journal*, 835, 268  
 Kahil, F., Hirzberger, J., Solanki, S. K., et al. 2022, *A&A*, 660, A143  
 Lemen, J., Title, A., Akin, D., et al. 2012, *Solar Physics*, 275, 17  
 Lezzi, S. M., Andretta, V., Murabito, M., & Del Zanna, G. 2023, *A&A*, 680, A61  
 Lezzi, S. M., Long, D. M., Andretta, V., et al. 2024, *A&A*, 690, A342  
 Morgan, H. & Druckmüller, M. 2014, *Sol. Phys.*, 289, 2945  
 Müller, D., St. Cyr, O. C., Zouganelis, I., et al. 2020, *A&A*, 642, A1  
 Munro, R. H. & Withbroe, G. L. 1972, *ApJ*, 176, 511  
 Nölke, J. D., Solanki, S. K., Hirzberger, J., et al. 2023, *A&A*, 678, A196  
 Payne, A. V. & Sun, X. 2021, *ApJ*, 912, 1  
 Pesnell, W. D., Thompson, B. J., & Chamberlin, P. C. 2012, *The Solar Dynamics Observatory (SDO)*, ed. P. Chamberlin, W. D. Pesnell, & B. Thompson (New York, NY: Springer US), 3–15  
 Peter, H., Bingert, S., & Kamio, S. 2012, *A&A*, 537, A152  
 Rochus, P., Auchère, F., Berghmans, D., et al. 2020, *A&A*, 642, A8  
 Sakao, T., Kano, R., Narukage, N., et al. 2007, *Science*, 318, 1585  
 Schou, J., Scherrer, P. H., Bush, R. I., et al. 2012, *Sol. Phys.*, 275, 229  
 Singh, T., Sterling, A. C., & Moore, R. L. 2021, *The Astrophysical Journal*, 909  
 Sinjan, J., Calchetti, D., Hirzberger, J., et al. 2022, in *Society of Photo-Optical Instrumentation Engineers (SPIE) Conference Series*, Vol. 12189, Software and Cyberinfrastructure for Astronomy VII, 121891J  
 Solanki, S. K., del Toro Iniesta, J. C., Woch, J., et al. 2020, *A&A*, 642, A11  
 SPICE Consortium, Anderson, M., Appourchaux, T., et al. 2020, *A&A*, 642, A14  
 St. John, C. E. 1911, *ApJ*, 34, 57

- Stansby, D., Yeates, A., & Badman, S. T. 2020, *Journal of Open Source Software*, 5, 2732
- The SunPy Community, Barnes, W. T., Bobra, M. G., et al. 2020, *The Astrophysical Journal*, 890, 68
- Waldmeier, M. 1956, *Zeitschrift für Astrophysik*, 38, 219
- Waldmeier, M. 1957, *Die Sonnenkorona 2*. Birkhäuser Verlag Basel und Stuttgart
- Wang, Y. M., Robbrecht, E., & Muglach, K. 2011, *ApJ*, 733, 20
- Wiegelmann, T. & Solanki, S. K. 2004, *Solar Physics*, 225, 227
- Yeates, A. 2020, Numerical methods — pfsspy documentation, [https://pfsspy.readthedocs.io/en/latest/numerical\\_method.html](https://pfsspy.readthedocs.io/en/latest/numerical_method.html), accessed: 2025 August 20
- Zhang, J., Yang, S., Liu, Y., & Sun, X. 2012, *The Astrophysical Journal Letters*, 760, L29

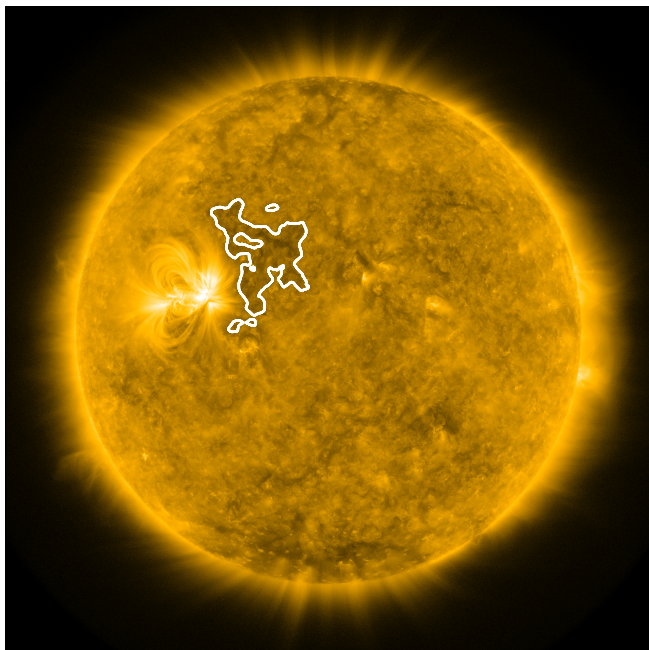


**Fig. A.1.** SDO/AIA 171Å observation of 2018 April 22 19:24. The dark halo adjacent to AR NOAA 12706 is outlined in white.

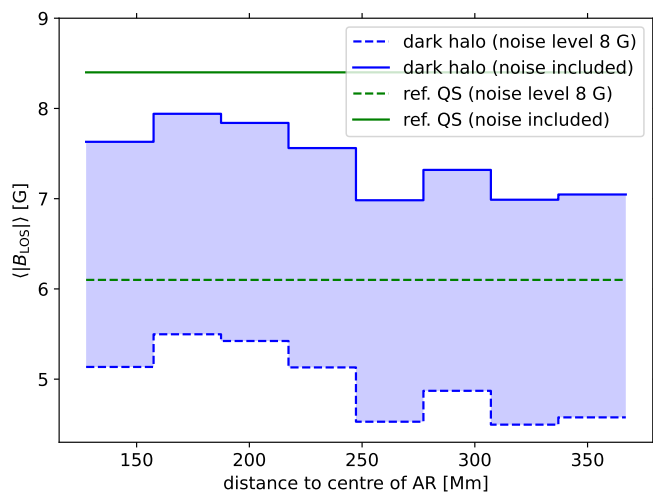


**Fig. A.2.** The  $\langle |B_{\text{LOS}}| \rangle$  in dependence of distance to the AR centre for the 2018 April 22 SDO observations. We show the  $\langle |B_{\text{LOS}}| \rangle$  inside the dark halo in blue calculated in two ways: The dashed line indicates the treatment where all pixels below the noise level have been set to zero, and the solid line displays the case where pixels below the noise levels have also been included. The shaded area indicates the range of these two calculations giving the maximum uncertainty range for the real unsigned magnetic flux density. The  $\langle |B_{\text{LOS}}| \rangle$  for the QS is given in green.

## Appendix A: SDO 2018 April 22 data set

We studied the same SDO data set from 2018 April 22 19:24 (with the HMI magnetogram from 19:24:24, and the three AIA channels at 171Å, 193Å, and 211Å from 19:24:09, 19:24:04, and 19:24:09, respectively) as Lezzi et al. (2023). It contains AR NOAA 12706 and a dark halo adjacent to it in the west (see Fig. A.1). We aim to analyse the photospheric magnetic field of this dark halo and compare the results to the dark halos analysed in Sect. 4.3.2 and by Lezzi et al. (2023). For this purpose

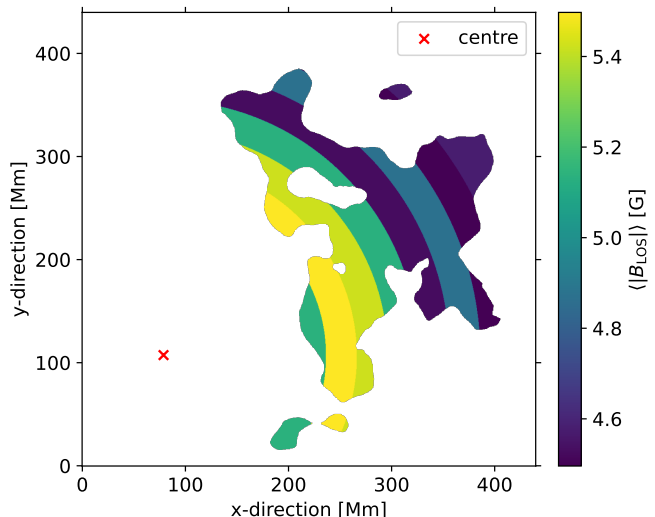


**Fig. A.3.** The  $\langle |B_{\text{LOS}}| \rangle$  inside concentric rings around the AR given as a function of distance to the AR centre for the SDO observations taken on 2018 April 22 19:24.

we produced level 1.5 data for the 171Å observation and additionally normalised the intensity to DN/s by dividing the image by the exposure time. The co-temporal SDO/HMI LOS magnetogram was re-projected to the SDO/AIA image using the SunPy reproject package.

In order to reproduce the dark halo contours in Lezzi et al. (2023) we tested different filters and filter settings for convolving the SDO/AIA 171Å image from which smooth iso-contours of the dark halo can be obtained. A uniform filter with a size of 40 pixels yields the closest result to theirs. We first convolved the 171Å image with this uniform filter and then applied a 55% mean disc intensity threshold to identify the dark halo next to the AR NOAA 12706. These contours are very similar to the ones that can be obtained by convolving the image with a Gaussian filter and then applying an intensity-threshold of 75% of the mean QS intensity at disc centre (as has been done in Sect. 3.1). We also selected the same reference QS area in the north-east of the solar disc which has a size of  $250'' \times 337''$ .

We applied the same noise level of 8 G as used by Lezzi et al. (2023) to derive the unsigned magnetic field,  $B_{\text{unsigned}}$ , by averaging the absolute values in the pixels above this noise level. We obtained  $B_{\text{unsigned}} = 15.6$  G in the dark halo and  $B_{\text{unsigned}} = 16.1$  G in the QS. The QS value compares well to the one presented in Lezzi et al. (2023), however, the value for the dark halo is 1.4 G lower than theirs.

To better compare these values with the 2021 November 8 Solar Orbiter data set, we calculated the corresponding unsigned magnetic flux densities,  $\langle |B_{\text{LOS}}| \rangle$ , (according to Eq. 2). We applied the same noise level of 8 G and derived a lower limit for the unsigned magnetic flux density by setting pixels below the noise level to zero. This way we obtained an unsigned magnetic flux density of 5.0 G for the dark halo and the higher value of 6.1 G for the QS. This result is consistent with our previous findings for the 2021 November 5 Solar Orbiter observations in the sense that the  $\langle |B_{\text{LOS}}| \rangle$  in the DH is somewhat lower than in the QS. From Fig. A.2 it follows that this is the case at every distance from the centre of the neighbouring AR, irrespectively of whether we consider the upper or the lower limit of the flux density.

In the same way as for the 2021 November 5 Solar Orbiter observation, we calculated the  $\langle |B_{\text{LOS}}| \rangle$  inside concentric rings around the AR. We derived the centre of the AR by computing the geometric centre of magnetic elements with field strengths above 100 G within an area of  $\sim 175$  Mm (400 pixels) around the clearly visible leading sunspot. As in Sect. 4.3.2 we calculated the  $\langle |B_{\text{LOS}}| \rangle$  inside each concentric ring with a width of 30 Mm starting at  $\sim 130$  Mm (290 pixel). Like in Sect. 4.3.2 we derived  $\langle |B_{\text{LOS}}| \rangle$  in two ways: by considering only signals above the noise level are solar (i.e. setting all signals hidden in the noise to zero), and by assuming that pixels below the noise level show signal (i.e. assuming that the noise is zero). This is shown in Fig. A.3.

Although only a relatively weak decrease in the unsigned magnetic flux density from the inner to the outer boundaries of this dark halo is observed, the magnetic field tends to decrease with distance from the AR. This  $\langle |B_{\text{LOS}}| \rangle$ –distance dependence is shown in Fig. A.2. In the ring closest to the AR centre the dark halo has a value of 5.1 G (considering the noise corrected values), which rises to 5.5 G inside the next ring, but then starts to decrease showing some variation in this trend. At the outer edge of the dark halo  $\langle |B_{\text{LOS}}| \rangle$  has reached 4.6 G. This general trend agrees with that already observed in the 2021 November 5th Solar Orbiter observations (see Fig. 9). The difference between the dark halo and the QS is, however, more pronounced in this data set: The QS is with 6.1 G well above the  $\langle |B_{\text{LOS}}| \rangle$  inside the dark halo at all distances from the AR.